

Cite this: *Nanoscale*, 2014, **6**, 9774

Quantitative synchrotron X-ray fluorescence study of the penetration of transferrin-conjugated gold nanoparticles inside model tumour tissues

Tianqing Liu,^a Ivan Kempson,^a Martin de Jonge,^b Daryl L. Howard^b and Benjamin Thierry^{*a}

The next generation of therapeutic nanoparticles in the treatment of cancer incorporate specific targeting. There is implicit importance in understanding penetration of targeted nanomedicines within tumour tissues via accurate and quantitative temporospatial measurements. In this study we demonstrate the potential of state-of-the-art synchrotron X-ray fluorescence microscopy (XFM) to provide such insights. To this end, quantitative mapping of the distribution of transferrin-conjugated gold nanoparticles inside multicellular tumour spheroids was achieved using XFM and compared with qualitative data obtained using reflectance confocal microscopy. Gold nanoparticles conjugated with human transferrin with a narrow size-distribution and high binding affinity to tumour cells were prepared as confirmed by cellular uptake studies performed on 2D monolayers. Although the prepared 100 nm transferrin-conjugated gold nanoparticles had high targeting capability to cancer cells, penetration inside multicellular spheroids was limited even after 48 hours as shown by the quantitative XFM measurements. The rapid, quantitative and label-free nature of state-of-the-art synchrotron XFM make it an ideal technology to provide the structure–activity relationship understanding urgently required for developing the next generation of immuno-targeted nanomedicines.

Received 18th April 2014
Accepted 9th May 2014

DOI: 10.1039/c4nr02100b
www.rsc.org/nanoscale

Introduction

Accurate and quantitative determination of the spatial distribution of nano-sized materials within tissues is of high importance towards understanding their interactions with biological entities and fate in biological systems. Ultimately this knowledge is required to establish their safety profile as well as to optimize therapeutic or diagnostic efficacy of nanomedicine agents currently under development. Of particularly high importance is the understanding of the penetration of nanoparticles within interstitial tumour tissues. Limited drug penetration within tumour tissues and inhomogeneous interstitial distribution play a major role in the resistance of metastatic cancers to standard chemotherapy.^{1–4} Penetration of chemotherapeutic drugs in cancerous tissues is mostly controlled by their intrinsic physicochemical properties such as molecular weight and lipophilicity.² Not surprisingly, the physicochemical properties of nanoparticles control to an even greater extent than for chemotherapeutics their ability to penetrate tumour tissues.^{5,6} Nanoparticles functionalized with biological ligands of high binding affinity to tumour cells are widely expected to be the next generation of therapeutic

nanoparticles, and are currently undergoing pre-clinical validation. Recent studies endeavoured to elucidate the transport of such immune-constructs within tumour tissues.^{7–9} However quantitative technology capable of accurately mapping the distribution of nanoparticles in tumour tissues is lacking, which is a serious obstacle to obtain the required understanding.

Gold nanoparticles are of high interest in nanomedicine owing to their optical properties such as the ability to support localized surface plasmon resonance (LSPR) and their excellent Rayleigh scattering efficiency in the visible range. These unique optical properties have been exploited towards the development of a number of biodiagnostic and therapeutic applications.^{10,11} Beside their intrinsic properties and well-established biocompatibility, the use of gold nanoparticles as a model in mechanistic studies is advantageous due to the existence of well-established synthetic routes providing excellent control over their size and shape. Using *in vitro* 3D tumour models that recapitulate the physicochemical and biological aspects relevant to nanomedicine transport, the effect of nanoparticles' hydrodynamic size on penetration has been studied.¹² Similarly, gold nanoparticles used as a model provided mechanistic information on the effect of surface charges on tumour tissue penetration in an *in vitro* tumour spheroid model.¹³ The predominance of plasmonic scattering effects over absorption ones for gold nanoparticles above 20 nm in diameter enables

^aIan Wark Research Institute, University of South Australia, Mawson Lakes Campus, Mawson Lakes, Adelaide, SA 5095, Australia. E-mail: Benjamin.Thierry@unisa.edu.au

^bAustralian Synchrotron, Clayton, Victoria 3168, Australia

their direct observation in the reflectance mode of confocal microscopy, providing efficient visualization in biological systems at the single nanoparticle level.^{14,15} Confocal microscopy-based imaging remains however poorly quantitative, especially in heterogeneous tissues.

Recent progress in efficiency of X-ray fluorescence detectors (XRF)^{16,17} coupled to synchrotron radiation sources has given rise to ultra-fast XRF mapping, generating images on time scales up to three orders of magnitude faster than previously possible for a comparable pixel number. This new capability is revolutionizing the ability of acquiring biologically and statistically relevant quantitative data. Specifically X-ray fluorescence microscopy (XFM) can image metal (*e.g.* Au, Fe, Gd) distributions in biological materials with high sensitivity over large sample areas/numbers and therefore is ideal to study distributions of unlabelled nanoparticles as a function of multiple variables.¹⁸ XFM has been used to map 2D projected elemental distributions over length scales ranging from under 1 μm to tens of millimetres, covering cells, small multicellular organisms, and larger sectioned specimens. The specific aspects of synchrotron based XFM include a high sensitivity, enabling elemental mapping at ppm–ppb concentrations, and a very rapid acquisition potential due to the large detector solid angle, resulting in high experimental efficiency, and the high intensity of the probe beam. The excellent potential of XFM to provide mapping of platinum drug distribution in spheroids has been demonstrated.^{19–21}

We report here for the first time on the use of synchrotron XFM to achieve quantitative mapping of the penetration of gold nanoparticles targeted to the transferrin receptor inside tumour tissues. To this end, 3D multicellular tumour spheroids were prepared and treated with the nanoparticles for various times. The quantitative XFM data are qualitatively in good agreement with those obtained using reflectance confocal microscopy.

Materials and methods

Materials

Chloroauric acid ($\text{HAuCl}_4 \cdot 3\text{H}_2\text{O}$), sodium citrate, *N*-hydroxy-succinimide (NHS), *N*-(3-dimethylaminopropyl)-*N'*-ethyl-carbodiimide hydrochloride (EDC), Phosphate Buffered Saline (PBS), and human holo-transferrin were obtained from Sigma-Aldrich and used as received from the manufacturer without further purification. Water used in the experiments was purified with a Millipore water treatment system (organic content less than 5 ppb). Polyethylene glycol thiol (HS-PEG-CH₃) with an average molecular weight of 5000 g mol⁻¹ was purchased from Rapp polymer GmbH. Short chain length PEG thiol acid (molecular weight 458.6) was purchased from Polypure.

Gold nanoparticle synthesis and surface modification

Gold nanoparticle synthesis and surface modification with PEG and targeting ligands have been carried out using the methods reported in our previous study.^{15,22} Briefly, gold nanoparticle seeds (~18 nm) were prepared using the standard citrate method. Larger gold nanoparticles (~100 nm) were prepared

from the gold nanoparticle seeds (51 μL) by adding 1% citrate solution (22 μL) and 0.03 M hydroquinone solution (100 μL) as reducing agents to the 1% HAuCl₄ solution to reach the final volume of 10 mL.²³ To prevent irreversible aggregation and increase the shelf life of nanoparticles, as-synthesized 100 nm gold nanoparticles were treated with a small amount of 0.05% (v/v) Tween 20 for 30 min. Tween 20, which is weakly physisorbed on gold nanoparticles, provides steric stabilization and can be gradually displaced by organothiols (*e.g.* thiolated PEG). After purifying the gold nanoparticles, mixed thiolated PEG molecules comprising carboxylic functionalized short chain length PEG molecules (Fw 458.6) and longer chain length PEG molecules (Fw 5000) with the ratio of 1 : 4 were used to stabilize the gold nanoparticles and enable optimal bioconjugation of monoclonal antibodies to the nanoparticles. The mixed PEG solution (1 mg mL⁻¹) was added to the gold nanoparticle solution under vortex and left to react for at least 6 hours at room temperature. After purification by centrifugation, the carboxyl groups on the PEGylated gold nanoparticles (1.0 mM, 1 mL) were activated using 100 μL of NHS (20 mg mL⁻¹) and EDC (15 mg mL⁻¹) for 5 min. The nanoparticle suspensions were then quickly centrifuged and resuspended into PBS (900 μL). Human holo-transferrin or bovine transferrin (0.5 mg mL⁻¹, 0.1 mL) was added rapidly to the activated gold nanoparticles and left to react at room temperature and stored at 4 °C after the reaction. The transferrin-conjugated nanoparticles were washed with PBS twice at 4 °C to remove unconjugated transferrin prior to use.

Characterization of gold nanoparticles

The morphology and size distribution of as-synthesized gold nanoparticles prepared on a copper grid were analysed using a Philips CM100 transmission electron microscope (TEM). The hydrodynamic diameter of the nanoparticles before and after the bioconjugation was measured *via* dynamic light scattering (DLS) using a Zetasizer Nano ZS System equipped with a 633 nm He-Ne laser (Malvern Instruments). UV-Vis spectra were recorded using a Varian Cary 5 UV-Vis-NIR spectrophotometer at room temperature.

Cellular uptake of the transferrin-functionalized gold nanoparticles

To confirm the active targeting of human transferrin-functionalized gold nanoparticles, an *in vitro* cellular uptake study was carried out using MCF-7 human breast cancer cells. MCF-7 cells were cultured in complete medium, Dulbecco's Modified Eagle's Medium (DMEM, Invitrogen) supplemented with glutamine, 10% (v/v) fetal bovine serum (FBS), and 1% (v/v) penicillin/streptomycin. Cells were cultured in T-75 flasks in a humidified incubator at 37 °C, 5% CO₂ and 100% humidity. Subculture was performed every week. MCF-7 cells were harvested and cultured in a commercially made silicone well chamber device (Sarstedt, Germany) with a poly-L-lysine pre-coated glass surface. The seeding density of cells was 10 000 cells per well. After 24 h cell culture, the cells were washed with fresh DMEM medium and incubated for 2 h at 37 °C with

human transferrin-conjugated gold nanoparticles, bovine transferrin-conjugated gold nanoparticles, or PEGylated gold nanoparticles as a control at a gold concentration of 0.04 mM. Cells were extensively washed with PBS, fixed in a formalin solution (10% formaldehyde) at room temperature for 10 min, and then washed (3×1 mL). The cellular uptake of the nanoparticles was visualized using a Nikon inverted light microscope operating in bright field under a high magnification (100 \times objective, oil-immersion bright field condensers) and a reflectance confocal microscope (LSM510, Zeiss) as described previously.^{15,22} Triplicate samples were used for each analysis and each test was repeated three times.

Cell culture and formation of tumour spheroids

MCF-7 tumour spheroids were formed using custom-made polydimethylsiloxane (PDMS) microwells. Briefly, the PDMS microwell devices were replicated from a microwell mould after baking at 65 °C for 2 h. The surface of the PDMS microwells was passivated using Pluronic F127 (1% w/v in water) treatment to repel cells from attaching to the surface. The devices were balanced with cell culture medium for 30 min before cell seeding. Cancer cell suspensions of MCF-7 cancer cells (400 μ L) were seeded into the devices and flowed into each microwell. The cell sedimentation was assisted by vibrating gently. The medium was removed every two days and refilled with fresh medium. The device was kept in an incubator for ten days' cell culture to obtain tumour spheroids with the diameter of around 500 μ m. The growth of the spheroids was monitored using an inverted microscope (Nikon Eclipse TE, Japan). The obtained spheroids were fixed with 4% formaldehyde for 1 h and permeabilized with 0.1% Triton X-100 in PBS for 1 h. The F-actin and nuclei of the cells were then stained with rhodamine phalloidin (50 μ g mL⁻¹) and DAPI (1 μ g mL⁻¹) in the dark at room temperature for 1 h. After being washed with PBS to remove the extra fluorescent dyes, spheroids were imaged with an inverted Nikon A1R laser scanning confocal microscope. The spheroids were scanned in the z-direction with a step size of 2 μ m to identify the centre of the spheroids and acquire images.

Gold nanoparticle treatment of the multicellular tumour spheroids

MCF-7 tumour spheroids with an average diameter of 500 μ m were incubated with transferrin-conjugated gold nanoparticles at a final concentration of 0.04 mM for 2, 12 and 48 h. The treated tumour spheroids harvested from the microwell devices were transferred into a 1.5 mL centrifuge tube and washed thoroughly with PBS (3×1 mL). The spheroids were fixed in a formalin solution (4% formaldehyde) at room temperature and washed (3×1 mL) with PBS. The spheroids were embedded in optimal cutting temperature compound (O.C.T., Tissue-Tek) by snap-freezing. Cryosections were collected using a cryostat (Leica, Germany) set to slices with 20 μ m thickness onto a glass coverslip for confocal microscopic imaging or onto a Kapton film (7 μ m) for XRF analysis. Spheroid tissue sections were freeze-dried at -45 °C for 16 hours and kept under dry conditions until imaging.

Gold nanoparticle distribution imaging by reflectance confocal microscopy

The distribution of transferrin-conjugated gold nanoparticles in spheroid tissue sections was firstly scanned with reflectance confocal microscopy (LSM510) using the same settings mentioned previously. Transmitted and reflectance images were acquired with a 10 \times objective. The penetration depth of the nanoparticles in the spheroid sections was obtained from the intensity profiles of the reflectance channel after image acquisition. The largest section of each spheroid was used for scanning. Three samples were measured for each condition.

Quantitative gold nanoparticle mapping using synchrotron X-ray fluorescence microscopy

Gold nanoparticle distribution in the spheroid sections was mapped quantitatively at the X-ray fluorescence microscopy beamline at the Australian Synchrotron.²⁴ Quantitative gold penetration data inside the spheroids at different incubation time points were averaged from 6 radial profiles randomly chosen. A Kirkpatrick-Baez mirror microprobe was used in conjunction with a Maia 384 detector array.^{16,25} Excitation was performed using an X-ray beam with a flux of 2×10^{10} photons per second at 15.71 keV focused to a $2 \times 2 \mu\text{m}^2$ spot size. Dwell times of 0.5–10 ms were used depending on the sample and the concentration of the element of interest. Measurement of a Platinum XRF standard foil (Micromatter) was used to establish elemental quantitation. Spectra from XFM maps were fitted using GeoPIXE and elemental concentrations determined using a fundamental parameter approach,¹⁶ and a standard cellulose matrix set to a thickness of 20 μ m.

While the fundamental parameter approach can be susceptible to substantial errors in quantitation resulting from the extrapolation over a wide range of energy of small discrepancies in modelled parameters, in this case the errors were minimised by using the Pt L-shell fluorescence for the quantitation of Au using L-shell emission. The energy difference of these two emissions caused a negligible error relative to that of the real density of the Pt reference foil, which was stated as 5% absolute accuracy. The use of foil standards is only accurate when the absorbing matrix of the unknown specimen is negligible; in this case, the 20 μ m thick specimens (thinner when dried) are estimated to absorb no more than around 1.3% of the most intense of the gold L-lines, Au L-alpha_1, at around 9.713 keV. We have used the cellulose matrix ($\text{C}_6\text{H}_{10}\text{O}_5$, density 1.5 g cm⁻³) to estimate the specimen absorption, and the error of this assumption is likely to be below around 50%. We therefore estimate the Au quantitation reported in this article to be accurate to around 5%.

Results and discussion

Synthesis and characterization of human transferrin-conjugated gold nanoparticles

Gold nanoparticles were used as a model system to understand the penetration of transferrin-targeted nanoparticles inside multicellular tumour spheroids, taking advantage of their scalable synthesis methods with tunable dimensions, the

unique optical properties and good biocompatibility.^{26–28} In addition, gold is a xenobiotic element in tumour biological environments, making it possible to accurately quantify the gold nanoparticles in cancer cells and tumour tissues. Large gold nanoparticles were synthesized based on the citrate and hydroquinone reduction method.²³ The size of the as-synthesized gold nanoparticles was precisely controlled (around 95 ± 3 nm), as confirmed by TEM measurement (Fig. 1A). This size of the nanoparticles is the range of most therapeutic nanomedicine agents approved or under development. For instance, the FDA-approved anti-cancer nanomedicine Doxil has an average diameter of 90–100 nm.²⁹

The surface biofunctionalization of the gold nanoparticles has been well optimized in our previous work.^{15,22} Human holotransferrin is selected here as the targeting ligand because it is a well-recognized ligand and has been used in human clinical trials for cancer targeting.^{30,31} Transferrin conjugation with gold nanoparticles was carried out by the covalent coupling of the carboxylic moieties on the PEG adlayer with the primary amines of human transferrin *via* carbodiimide chemistry. Gold nanoparticles were first PEGylated with an optimized layer of mixed thiolated PEGs (molecular weight 5000 and 458.6 with the mixed ratio of 4 : 1). Long PEG chains with a molecular weight of 5000 and a –CH₃ terminal were used to provide steric stability to the gold nanoparticles under physiologically relevant conditions (*i.e.* high ionic strength cell culture medium) as well as

during the bioconjugation procedure, while the low molecular weight PEG chains provide high density of conjugation sites.²² The nanoparticles were characterized by DLS and UV-Vis spectroscopy to confirm their colloidal stability and successful surface modification. There were no significant differences in localized surface plasmon resonance peaks in the UV-Vis spectrum (Fig. 1B), suggesting good colloidal stability after conjugation. Using DLS, the hydrodynamic size shifts of the nanoparticles before and after transferrin conjugation were determined as a 12 nm diameter increase for 100 nm gold nanoparticles. These results are in agreement with our previously published report.²² Surface chemistry and stability in the biological environment are important for evaluating the behaviour of the nanoparticles in tumour models. The well-defined functionalized gold nanoparticles are suitable for the proposed mechanistic study.

Uptake of transferrin-conjugated gold nanoparticles by tumour cells

The *in vitro* cellular uptake of human transferrin-conjugated gold nanoparticles to the human breast adenocarcinoma cell line MCF-7 was determined by both bright field and reflectance confocal microscopic imaging. The percentages of cells positively labelled were quantified by inverted light microscopic images (Fig. 2A). Compared with both bovine transferrin-conjugated gold nanoparticles and PEGylated gold nanoparticles used as controls, there were significantly higher amounts of cancer cells which bound and internalized human transferrin gold nanoparticles (up to ~100% increase). On the other hand, minimal cellular uptake of the bovine transferrin-conjugated gold nanoparticles and PEGylated gold nanoparticles (less than 10%) was observed, confirming the specificity and efficiency of the biofunctionalization design used in this study. To obtain the three dimensional intracellular locations of the total nanoparticles at the single cell level, cells were also imaged with reflectance confocal microscopy which provided higher imaging quality and sensitivity. In agreement with bright field microscopy, more transferrin gold nanoparticles were clearly observed on each single cell in reflectance images (Fig. 2B). These results indicated the high binding affinity of the transferrin-conjugated nanoparticles, which was in good agreement with transferrin-enabled clathrin-mediated endocytosis reported in different cancer cell lines which over-express transferrin receptors³² or using other transferrin-based nanomedicine systems.^{33–35}

Penetration of transferrin-functionalized gold nanoparticles inside tumour spheroids

The transport of nanoparticles inside tumour micro-tissues is controlled to a large extent by their physicochemical properties.^{5,13,36,37} The poor penetration of anti-cancer drugs inside tumour tissues is associated with low therapeutic efficacy and recurrence of tumours. It is therefore of paramount importance to understand the parameters controlling the tumour penetration of nanoparticles towards designing nanomedicine agents with improved therapeutic profiles. Here, we evaluated in an *in*

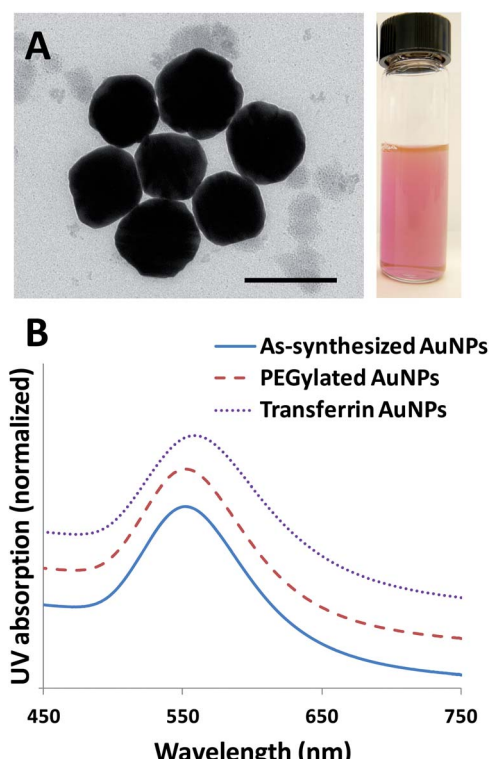


Fig. 1 Characterization of gold nanoparticles. (A) A TEM image of the as-synthesized gold nanoparticles (AuNPs) and the corresponding solution (right). The scale bar is 100 nm. (B) UV-visible absorption spectra of the as-synthesized, PEGylated, and transferrin-conjugated AuNPs.

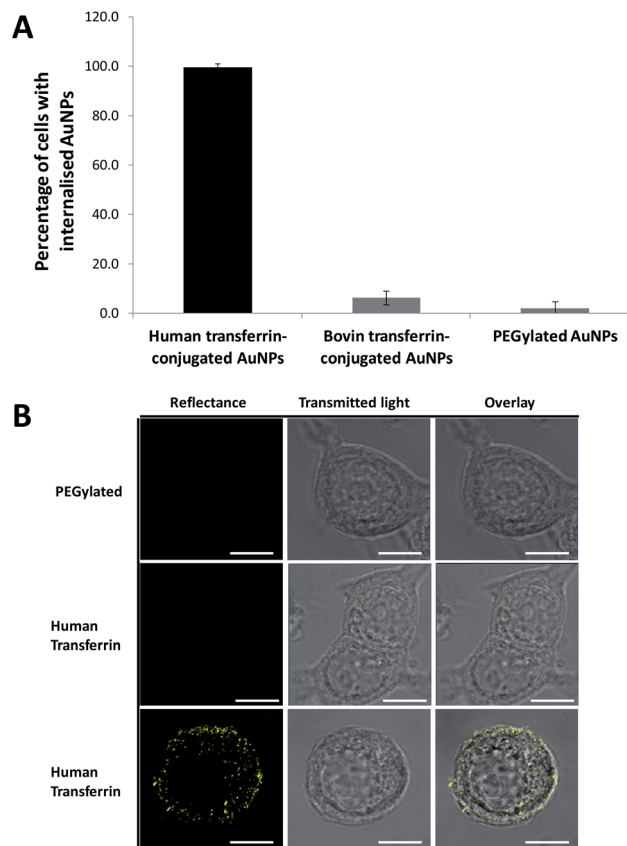


Fig. 2 Cellular uptake of 100 nm AuNPs by MCF-7 cancer cells. (A) Percentage of cells with internalised nanoparticles for human transferrin-conjugated AuNPs, bovine transferrin-conjugated AuNPs, and unconjugated PEGylated AuNPs. The data are calculated from 10 different images captured by light microscopy. (B) Confocal microscopic images (bright field, reflectance and their overlay) of human transferrin-conjugated AuNPs, bovine transferrin-conjugated AuNPs, and PEGylated AuNPs associated with a single cell. The scale bars are 10 μm .

vitro 3D model the transport of 100 nm gold nanoparticles conjugated with human transferrin, a ligand strongly expressed on most tumour cells. 3D tumour spheroid models mimic avascular interstitial tumour regions in solid tumours.^{38,39}

MCF-7 tumour spheroids formed using custom made microfabricated concave microwells. To verify their suitability

for the proposed study, the spheroids were first stained for actin and nuclei with fluorescent dyes (rhodamine phalloidin and DAPI respectively). The confocal microscopic images of the spheroids (Fig. 3) confirmed the expected morphology and closely packed cell structure with uniformly distributed actin filaments suggesting an intact cytoskeleton and cell–cell junctions. Next, the tumour spheroids were incubated with transferrin-functionalized gold nanoparticles (100 nm) for 2, 12 or 48 hours. To precisely map the distribution and determine the penetration depth of the nanoparticles, cryosectioning was employed to obtain tissue sections with a thickness of 20 μm . Tumour spheroid sections were imaged using either reflectance confocal microscopy or XFM. Reflectance confocal microscopy, which relies on the high scattering of gold nanoparticles, does not require fluorophore labelling of the nanoparticles, which can potentially modify the nanoparticles' bio-interface and in turn influence their behaviour in contact with cells and tissues.

For these 100 nm human transferrin-conjugated gold nanoparticles, penetration inside tumour spheroids was dependent on the incubation time (Fig. 4). At 2 h post-treatment, bright spots in the reflectance images indicated a heterogeneous distribution of human transferrin-conjugated gold nanoparticles in the outer region of spheroids. The uptake of gold nanoparticles in the spheroids at the 2 h time point was low and non-uniform. At 12 h treatment, there was a clear uniform binding boundary formed around the spheroids, suggesting more homogenous uptake. The penetration boundary in the outer region increased with prolonged incubation time up to 48 h. The penetration boundary was approximately 50 μm after 48 h nanoparticle incubation. This indicated that as the incubation time increased, more human transferrin-conjugated gold nanoparticles bound to the cells in the outer region of the spheroids. Importantly, the limited penetration observed in this work, in good agreement with related previous studies, confirmed the validity of using avascular multicellular spheroid models since the presence of hypoxic tissues with ill-defined characteristics such as cellular densities is not expected to influence the intratumoural transport.

Although reflectance confocal microscopy provides useful mechanistic information qualitatively, it is challenging to obtain quantitative data even in a spheroid model with radial symmetry. In order to obtain quantitative information of the

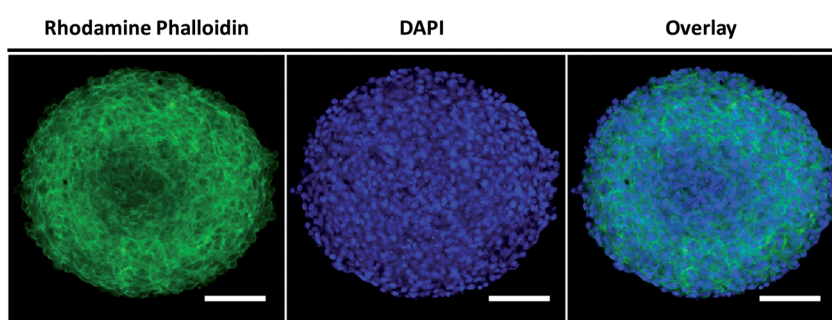


Fig. 3 High resolution confocal imaging of spheroids stained with rhodamine phalloidin and DAPI after 10 days' culture. The scale bars are 100 μm .

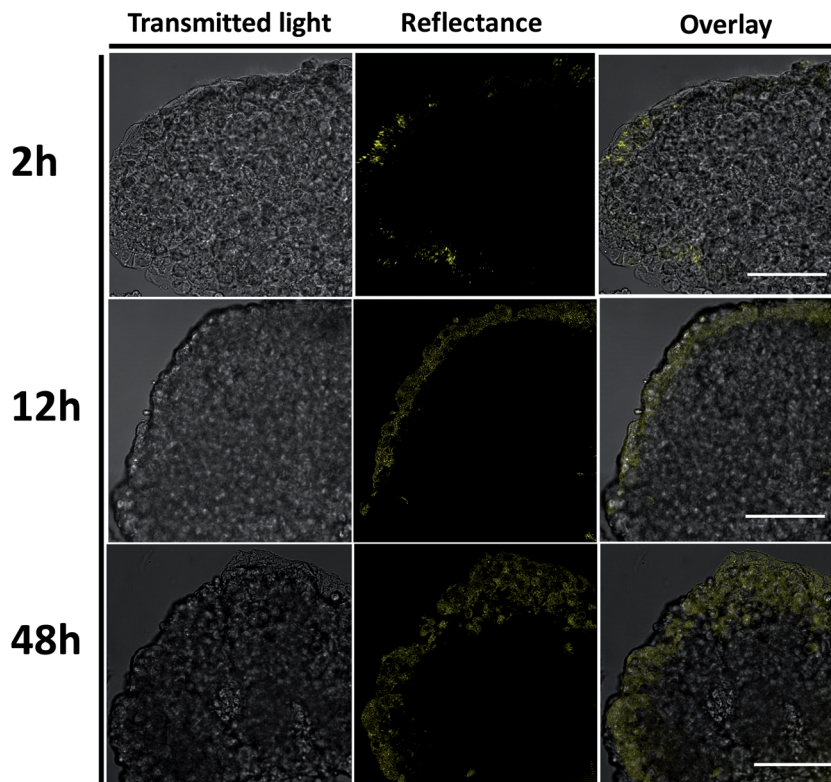


Fig. 4 Penetration behaviour of transferrin-conjugated AuNPs in MCF-7 tumour spheroids using reflectance confocal microscopy at time points of 2, 12, and 48 h. Nanoparticle treated spheroids were cryosectioned to 20 μm sections on glass substrates. Images were taken at different channels (bright field, reflectance and their overlay). The scale bars are 100 μm .

gold distributions within the tumour spheroids, synchrotron based X-ray fluorescence microscopy was used. Synchrotron XFM has an excellent elemental sensitivity and high spatial resolution, and a large field of view, and is therefore ideal for trace elemental mapping in biological tissues. Importantly, using the advanced set up at the Australian Synchrotron based on a Maia 384 detector array as initially reported by Ryan *et al.*,²⁵ ultrafast mapping could be acquired. The possibility of quantitatively mapping large tissue areas is a unique feature of advanced synchrotron XRF and a significant advancement in the field over the previously reported use of XRF, which was limited to small areas. Gold distribution maps in the spheroid sections were correlated with the Compton scattering channel used as a reference for tissues (Fig. 5A). Our previous studies revealed that a Compton map typically provides accurate information about the specimen structure and in good agreement with that of phase contrast images.²⁰ Quantification was conducted in the GeoPIXE software after calibration with foil standards and it is estimated that the Au mapping presented in this study is accurate to around 5%. In all the XRF images of sections from spheroids treated at different time points, gold signals had an inward radial symmetry from the edge of the spheroids. The penetration depth measured by XRM was compared with that determined by reflectance confocal microscopy. In both cases, the penetration depth increased over incubation time (Fig. 5B). However, even after 48 h incubation, the penetration depth as determined by XFM was limited to less

than 50 μm , in good agreement with the qualitative confocal study (Fig. 6).

Elucidating the transport of immuno-targeted nanoparticles in tumour tissues is of high importance towards optimizing their therapeutic index and developing the next generation of nanomedicines. This XFM study provides for the first time quantitative mapping of the distribution of such constructs in an advanced *in vitro* tumour model. The transport and binding of immuno-nanomedicines within solid tumours are directly controlled by their intrinsic physicochemical properties compounded by their binding affinity to tumour cells. Nanoparticles with hydrodynamic diameters around 100 nm have poor transport in the dense extracellular matrix of the interstitial space and consequently limited penetration within tumour tissues.^{12,40} However, recent reports suggest that targeting ligands on the nanoparticle surface can promote their tumour tissue penetration.^{7,9,41} For instance, folate targeting was shown in an *in vivo* model to lead to increased tumour accumulation, with endocytosis of the targeted nanocarriers contributing to their enhanced tumour retention. Mechanistic understanding about tumour penetration is however challenging considering the inherent multifactorial nature of *in vivo* tumour uptake, which includes extravasation from tumour neovasculature. In order to obtain greater insights into intratumoural transport mechanisms, studies on *in vitro* tumour models such as the one used here are useful. Using SKOV-3 multicellular spheroids and 100 nm silica nanoparticles targeted to the cell surface receptor

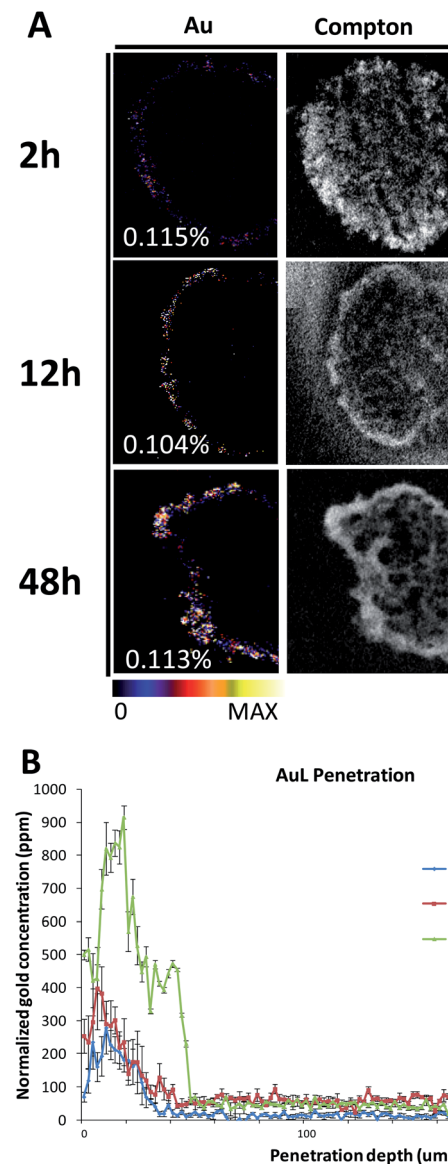


Fig. 5 XFM analysis of Au distribution of transferrin-conjugated AuNPs in MCF-7 tumour spheroids after 2, 12 and 48 h. (A) 2D elemental mapping of gold and Compton scattering. Maximal gold concentrations are displayed at the bottom left corner of each element map. (B) Quantitative radial gold concentration profiles of the spheroids treated at different time points.

CD44 through a hyaluronan ligand, El-Dakdouki *et al.* reported significantly improved penetration after 18 hours and related it to transcytosis.⁹ Although only one time point was used in this qualitative study, our quantitative study is in good agreement with El-Dakdouki *et al.* A clear time-dependant increase in spheroid penetration of transferrin-conjugated gold nanoparticles was determined and comparable penetration in the tumour tissue mimics, in the 50 μm range, was observed at the longer time point. At the molecular level, conjugation of holotransferrin (the form of human transferrin loaded with iron) to gold nanoparticles enables strong binding to transferrin receptors overexpressed on tumour cells ($K_d = 1\text{--}10 \text{ nM}$). After a series of cellular vesicle activity, cells can release the apo-

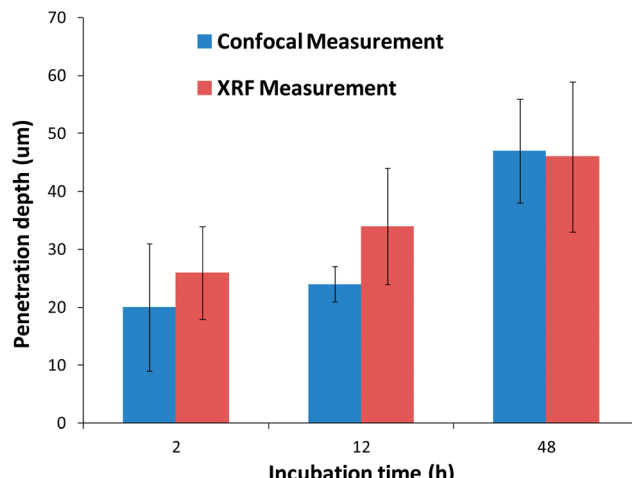


Fig. 6 Comparison of penetration depth of transferrin-conjugated AuNP treated spheroids measured by confocal microscopy and synchrotron XRF imaging.

transferrin nanoparticles and regenerate the transferrin receptors.^{42,43} We can therefore hypothesize that dynamic transport events are involved in the penetration of functionalized nanoparticles inside tumour micro-tissues, although further studies are warranted to fully investigate the mechanisms at play. If confirmed *in vivo*, limited penetration of nanoparticles inside tumour tissues would be a major issue as delivery to hypoxic areas deep inside solid tumours is of high therapeutic importance. The data presented in this study demonstrate that synchrotron XFM is an excellent technology to address these important questions and quantitatively map the distribution of un-labelled nanoparticles in tumour tissues.

Conclusion

In summary, this study demonstrates the ability of state-of-art synchrotron based X-ray fluorescence microscopy to achieve high spatial-resolution and quantitative elemental mapping of nanoparticles in biological tissues. Using 3D multicellular tumour spheroids as a tumour tissue model, the intra-tumoural penetration behaviour of 100 nm transferrin-conjugated nanoparticles was determined qualitatively by reflectance confocal and quantitatively using synchrotron XRF microscopies. In agreement with previous studies, the penetration of the 100 nm transferrin-conjugated gold nanoparticles was limited. With the imminent emergence of immuno-targeted nanomedicines in clinical practice, this structure-activity relationship urgently requires a more complete understanding and the rapid, quantitative and label-free nature of state-of-the-art synchrotron XFM make it an ideal technology to provide the desired mechanistic insights. Importantly, the high penetration of X-rays suits them ideally to the mapping of trace elements in thick biological samples with minimal specimen preparation, paving the way to reliable quantitative studies in tumour tissues.

Acknowledgements

This work was supported by the NH&MRC project grant 1045841 and the Australian Synchrotron. This work was performed in part at the South Australian node of the Australian National Fabrication Facility, a company established under the National Collaborative Research Infrastructure Strategy to provide nano and micro-fabrication facilities for Australian researchers.

References

- K. P. Olive, M. A. Jacobetz, C. J. Davidson, A. Gopinathan, D. McIntyre, D. Honess, B. Madhu, M. A. Goldgraben, M. E. Caldwell, D. Allard, K. K. Frese, G. DeNicola, C. Feig, C. Combs, S. P. Winter, H. Ireland-Zecchini, S. Reichelt, W. J. Howat, A. Chang, M. Dhara, L. Wang, F. Rückert, R. Grützmann, C. Pilarsky, K. Izeradjene, S. R. Hingorani, P. Huang, S. E. Davies, W. Plunkett, M. Egorin, R. H. Hruban, N. Whitebread, K. McGovern, J. Adams, C. Iacobuzio-Donahue, J. Griffiths and D. A. Tuveson, *Science*, 2009, **324**, 1457–1461.
- A. I. Minchinton and I. F. Tannock, *Nat. Rev. Cancer*, 2006, **6**, 583–592.
- S.-H. Kim, H.-J. Kuh and C. R. Dass, *Curr. Drug Discovery Technol.*, 2011, **8**, 102–106.
- K. N. Sugahara, T. Teesalu, P. P. Karmali, V. R. Kotamraju, L. Agemy, D. R. Greenwald and E. Ruoslahti, *Science*, 2010, **328**, 1031–1035.
- H. Cabral, Y. Matsumoto, K. Mizuno, Q. Chen, M. Murakami, M. Kimura, Y. Terada, M. Kano, K. Miyazono and M. Uesaka, *Nat. Nanotechnol.*, 2011, **6**, 815–823.
- C. Wong, T. Stylianopoulos, J. Cui, J. Martin, V. P. Chauhan, W. Jiang, Z. Popović, R. K. Jain, M. G. Bawendi and D. Fukumura, *Proc. Natl. Acad. Sci. U. S. A.*, 2011, **108**, 2426–2431.
- E. Vlashi, L. E. Kelderhouse, J. E. Sturgis and P. S. Low, *ACS Nano*, 2013, **7**, 8573–8582.
- A. Albanese, A. K. Lam, E. A. Sykes, J. V. Rocheleau and W. C. W. Chan, *Nat. Commun.*, 2013, **4**, 2718.
- M. H. El-Dakdouki, E. Pure and X. Huang, *Nanoscale*, 2013, **5**, 3904–3911.
- Y.-C. Yeh, B. Creran and V. M. Rotello, *Nanoscale*, 2012, **4**, 1871–1880.
- L. Dykman and N. Khlebtsov, *Chem. Soc. Rev.*, 2012, **41**, 2256–2282.
- T. Goodman, P. Olive and S. Pun, *Int. J. Nanomed.*, 2007, **2**, 265.
- B. Kim, G. Han, B. Toley, C. Kim, V. Rotello and N. Forbes, *Nat. Nanotechnol.*, 2010, **5**, 465–472.
- S. Klein, S. Petersen, U. Taylor, D. Rath and S. Barcikowski, *J. Biomed. Opt.*, 2010, **15**, 036015.
- T. Liu, A. Cousins, C.-C. Chien, I. Kempson, S. Thompson, Y. Hwu and B. Thierry, *Cancer Lett.*, 2013, **328**, 271–277.
- R. Kirkham, P. A. Dunn, A. J. Kuczewski, D. P. Siddons, R. Dodanwela, G. F. Moorhead, C. G. Ryan, G. de Geronimo, R. Beuttenmuller, D. Pinelli, M. Pfeffer, P. Davey, M. Jensen, D. J. Paterson, M. D. de Jonge, D. L. Howard, M. Kusel and J. McKinlay, *AIP Conf. Proc.*, 2010, **1234**, 240–243.
- C. G. Ryan, D. P. Siddons, R. Kirkham, P. A. Dunn, A. Kuczewski, G. Moorhead, G. de Geronimo, D. J. Paterson, M. D. de Jonge, R. M. Hough, M. J. Lintern, D. L. Howard, P. Kappen and J. Cleverley, *AIP Conf. Proc.*, 2010, **1221**, 9–17.
- I. M. Kempson, C. C. Chien, C. Y. Chung, Y. Hwu, D. Paterson, M. D. de Jonge and D. L. Howard, *Adv. Healthcare Mater.*, 2012, **1**, 736–741.
- R. A. Alderden, H. R. Mellor, S. Modok, M. D. Hall, S. R. Sutton, M. G. Newville, R. Callaghan and T. W. Hambley, *J. Am. Chem. Soc.*, 2007, **129**, 13400–13401.
- J. Z. Zhang, N. S. Bryce, R. Siegele, E. A. Carter, D. Paterson, M. D. de Jonge, D. L. Howard, C. G. Ryan and T. W. Hambley, *Integr. Biol.*, 2012, **4**, 1072–1080.
- J. Z. Zhang, N. S. Bryce, A. Lanzirotti, C. K. J. Chen, D. Paterson, M. D. de Jonge, D. L. Howard and T. W. Hambley, *Metalloomics*, 2012, **4**, 1209–1217.
- T. Liu and B. Thierry, *Langmuir*, 2012, **28**, 15634–15642.
- S. D. Perrault and W. C. W. Chan, *J. Am. Chem. Soc.*, 2009, **131**, 17042–17043.
- D. Paterson, M. D. de Jonge, D. L. Howard, W. Lewis, J. McKinlay, A. Starritt, M. Kusel, C. G. Ryan, R. Kirkham, G. Moorhead and D. P. Siddons, *AIP Conf. Proc.*, 2011, **1365**, 219–222.
- C. G. Ryan, D. P. Siddons, G. Moorhead, R. Kirkham, G. D. Geronimo, B. E. Etschmann, A. Dragone, P. A. Dunn, A. Kuczewski, P. Davey, M. Jensen, J. M. Ablett, J. Kuczewski, R. Hough and D. Paterson, *J. Phys.: Conf. Ser.*, 2009, **186**, 012013.
- G. Frens, *Nature*, 1973, **241**, 20–22.
- D. Pisswan, T. Niidome and M. B. Cortie, *J. Controlled Release*, 2011, **149**, 65–71.
- M. Thomas and A. M. Klibanov, *Proc. Natl. Acad. Sci. U. S. A.*, 2003, **100**, 9138–9143.
- A. Gabizon, H. Shmeeda and Y. Barenholz, *Clin. Pharmacokinet.*, 2003, **42**, 419–436.
- M. E. Davis, *Mol. Pharmaceutics*, 2009, **6**, 659–668.
- M. E. Davis, J. E. Zuckerman, C. H. J. Choi, D. Seligson, A. Tolcher, C. A. Alabi, Y. Yen, J. D. Heidel and A. Ribas, *Nature*, 2010, **464**, 1067–1070.
- J. Wang, S. Tian, R. A. Petros, M. E. Napier and J. M. DeSimone, *J. Am. Chem. Soc.*, 2010, **132**, 11306–11313.
- P.-H. Yang, X. Sun, J.-F. Chiu, H. Sun and Q.-Y. He, *Bioconjugate Chem.*, 2005, **16**, 494–496.
- J.-L. Li, L. Wang, X.-Y. Liu, Z.-P. Zhang, H.-C. Guo, W.-M. Liu and S.-H. Tang, *Cancer Lett.*, 2009, **274**, 319–326.
- L.-C. Wu, L.-W. Chu, L.-W. Lo, Y.-C. Liao, Y.-C. Wang and C.-S. Yang, *ACS Nano*, 2013, **7**, 365–375.
- B. R. Smith, P. Kempen, D. Bouley, A. Xu, Z. Liu, N. Melosh, H. Dai, R. Sinclair and S. S. Gambhir, *Nano Lett.*, 2012, **12**, 3369–3377.
- S. Perrault, C. Walkey, T. Jennings, H. Fischer and W. Chan, *Nano Lett.*, 2009, **9**, 1909–1915.
- D. V. LaBarbera, B. G. Reid and B. H. Yoo, *Expert Opin. Drug Discovery*, 2012, **7**, 819–830.

- 39 F. Hirschhaeuser, H. Menne, C. Dittfeld, J. West, W. Mueller-Klieser and L. A. Kunz-Schughart, *J. Biotechnol.*, 2010, **148**, 3–15.
- 40 H. Shuaidong, H. Ma, K. Huang, J. Liu, T. Wei, S. Jin, J. Zhang, S. He and X.-J. Liang, *Cancer Res.*, 2013, **73**, 319–330.
- 41 X. Wang, X. Zhen, J. Wang, J. Zhang, W. Wu and X. Jiang, *Biomaterials*, 2013, **34**, 4667–4679.
- 42 A. Dautry-Varsat, A. Ciechanover and H. F. Lodish, *Proc. Natl. Acad. Sci. U. S. A.*, 1983, **80**, 2258–2262.
- 43 D. T. Wiley, P. Webster, A. Gale and M. E. Davis, *Proc. Natl. Acad. Sci. U. S. A.*, 2013, **110**, 8662–8667.